Journal of Materials Science & Technology 82 (2021) 105–113

Contents lists available at ScienceDirect

Journal of Materials Science & Technology

journal homepage: www.jmst.org

Research Article

From thermal conductive to thermal insulating: Effect of carbon vacancy content on lattice thermal conductivity of ZrC_x

Yue Zhou*, William G. Fahrenholtz, Joseph Graham, Gregory E. Hilmas

Department of Materials Science and Engineering, Missouri University of Science and Technology, Rolla, MO 65409, USA

ARTICLE INFO

Article history:
Received 20 September 2020
Received in revised form 3 November 2020
Accepted 3 November 2020
Available online 20 January 2021

Keywords:
Zirconium carbide
Lattice thermal conductivity
Theoretical study
First-principle calculations

ABSTRACT

Lattice thermal conductivities of zirconium carbide (ZrC_x, $x = 1$, 0.75 and 0.5) ceramics with different carbon vacancy concentrations were calculated using a combination of first-principles calculations and the Debye-Callaway model. The Grüneisen parameters, Debye temperatures, and phonon group velocities were deduced from phonon dispersions of ZrC_x determined using first-principles calculations. In addition, the effects of average atomic mass, grain size, average atomic volume and Zr isotopes on the lattice thermal conductivities of ZrC_x were analyzed using phonon scattering models. The lattice thermal conductivity decreased as temperature increased for ZrC, $ZrC_{0.75}$ and $ZrC_{0.5}$ (Zr_2C), and decreased as carbon vacancy concentration increased. Intriguingly, ZrC_x can be tailored from a thermal conducting material for ZrC with high lattice thermal conductivity to a thermal insulating material for $ZrC_{0.5}$ with low lattice thermal conductivity. Thus, it opens a window to tune the thermal properties of ZrC_x by controlling the carbon vacancy content.

1. Introduction

Zirconium carbide (ZrC_x) is a promising candidate material for nuclear energy applications as a layer in tri-isotropic (TRISO) fuel particles [1], which are used in high-temperature gas-cooled reactors [2]. The main function of the ZrC_x layer is as a diffusion barrier for fission products from the kernel. Currently, SiC is the material of choice for such an application [3]. However, ZrC is stronger, which increases the crushing strength of ZrC-TRISO particles at elevated temperatures compared to SiC-TRISO particles [4]. In addition, ZrC is more stable than SiC under neutron irradiation at elevated temperatures [5,6], which increases the integrity of ZrC-TRISO fuel particles. Other potential applications of ZrC include heating elements in vacuum furnaces, coatings and matrices of ultra-high temperature ceramic matrix composites that could be used in hypersonic aerospace vehicles, rocket nozzles [7–11], and cutting tools [12–14].

For all the applications mentioned above, thermal conductivity plays a pivotal role. However, significant discrepancies exist among previously measured values of thermal conductivity of ZrC_x ceramics [15–19] as shown in Fig. 1. For example, in one study ZrC with a relative density of 93.3 % had a thermal conductivity range from 31 to 38 W m^{-1} K^{-1} at temperatures from 200 to 1000 °C [15]. In another study, ZrC with a relative density of 91.9 % had a thermal conductivity range from 18 to 26 W m^{-1} K^{-1} at temperatures from 300 to 1100 °C [14]. One possible reason for such differences is that these ZrC_x samples were prepared by different methods that resulted in different average grain sizes, carbon vacancy contents, and/or porosity levels/distributions and relative densities. Table 1 summarizes the preparation methods and characteristics of zirconium carbide ceramics from previous studies. The highest thermal conductivity values were reported for ZrC with larger grain sizes, lower carbon vacancy contents, and higher relative densities [13]. The typical room temperature thermal conductivity is about 30 W m^{-1} K^{-1}, depending on relative density [15].

In the Zr-C phase diagram, rock salt structured zirconium carbide is stable across a wide composition range and is represented by ZrC_x with x ranging from 0.98 to 0.63 (i.e., carbon vacancy contents from 0.02 to 0.37) [20]. The change of carbon content influences not only the lattice constant of ZrC_x, but also the thermal and mechanical properties. Previous studies demonstrated that the total thermal conductivity of ZrC_x decreased with increasing carbon vacancy content [21] due to the scattering of phonons and electrons by carbon vacancies. Likewise, theoretical studies [22,23] predicted that the elastic properties, Vickers hardness, and thermal conductivities of ZrC_x decreased with increasing carbon vacancy content. However,

* Corresponding author.
E-mail address: yznwb@mst.edu (Y. Zhou).

https://doi.org/10.1016/j.jmst.2020.11.068
1005-0302/

Table 1
Densification methods and sample characteristics of ZrC_x from previous studies sorted by highest to lowest thermal conductivity.

Ref.	Densification method	Composition	Relative density	Average grain size	Impurity Content	Thermal conductivity ($W\ m^{-1}\ K^{-1}$)
[13]	HP	$ZrC_{0.98}$	95%	50 μm	<0.2 wt.%	32.2, 600 °C
[16]	HP	$ZrC_{0.98}$	95%	50 μm	<0.2 wt.%	38.5, 1300 °C
[15]	SPS	ZrC	93.3 %	~10 μm	N/A	31.3, 200 °C
[17]	HP	ZrC	91.5 %	N/A	>0.165 wt.%	26.7, 1325 °C
[14]	HP	ZrC	91.9 %	3.7 μm	N/A	17.7, 300 °C

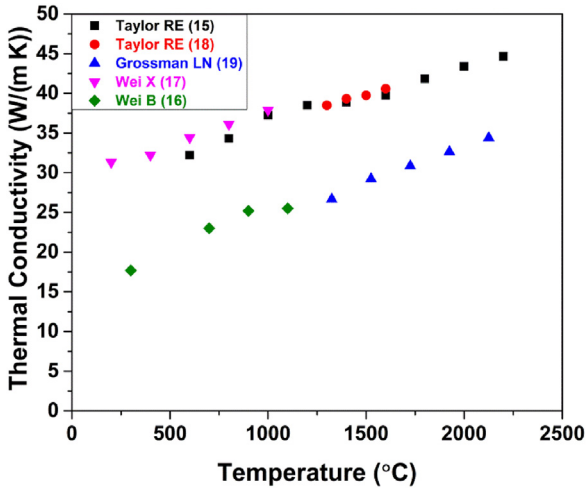

Fig. 1. Thermal conductivities of zirconium carbide measured in previous studies [15–19].

relatively few studies have been conducted using first-principles calculations to examine the lattice thermal conductivities of ZrC_x with different carbon vacancy contents. Molecular dynamics [24] and the Debye-Slack model [21] have been used to calculate the lattice thermal conductivities of ZrC_x with different carbon vacancy concentrations. However, the Debye-Callaway model has not been used to evaluate the effect of carbon vacancy on the lattice thermal conductivity of ZrC_x [25,26]. The effect of ordering of carbon vacancies on the lattice thermal conductivity was also investigated since the carbon vacancy ordered phase $ZrC_{0.5}$ has not only been predicted computationally [27,28] but also been observed experimentally [29,30]. However, because the carbon vacancy ordered Zr_2C always coexists with rock salt structured ZrC_x, its effect on the thermal conductivity of ZrC_x is difficult to determine experimentally. Thus, theoretical prediction of the lattice thermal conductivity of this ordered phase is needed.

ZrC_x is electrically conductive such that both electron and phonon transport contribute to thermal conductivity. As shown in Fig. 1, the total thermal conductivity of ZrC_x increases with increasing temperature, which is attributed to the increasing contribution of the electron contribution as temperature increases [31]. In addition, oxygen can dissolve into the ZrC_x lattice and is expected to be present in the carbon vacancy sites [32]. Furthermore, phonon scattering is expected to increase when impurity atoms are present [33] so that the phonon thermal conductivity of ZrC_x should decrease with increasing dissolved oxygen content. Thus, tailoring the thermal conductivity of zirconium carbide requires a deeper understanding of the mechanisms affecting the phonon transport in the lattice.

The Debye model is a statistical thermodynamic methodology to estimate the phonon contribution to heat capacity [34]. When the temperature (T) is much lower than the Debye temperature (θ_D), which is designated the "low" temperature regime, the model accurately predicts that heat capacity is proportional to T^3. In the low-temperature regime, the phonon group velocity (v) has a linear relationship with the frequency distribution of acoustic phonons and is expressed as $\omega = vq$, where ω is the phonon frequency, v is group velocity, and q is the wave vector of the phonon. Optical phonons are not active in the low-temperature regime. Likewise, the Debye model accurately predicts heat capacity in the "high" temperature limit where $T \gg \theta_D$ and the Debye model simplifies to the DuLong-Petit Law. However, at intermediate temperatures where both low and high-frequency phonons are active, the relationship between the acoustic phonon frequency and group velocity is no longer linear, leading to significant inaccuracies in the phonon frequency distribution predicted by the Debye model.

Klemens studied the statistical equilibrium of phonons with respect to temperature gradients and developed a general prediction for the thermal conductivity of dielectric solids with fixed equilibrium atom positions [35]. When atoms deviate from their ideal (i.e., absolute zero) positions, phonons scatter. The mean time between scattering events is defined as the relaxation time and different relaxation time can be determined for each phonon scattering process. Phonon scattering processes are typically divided into two main types: normal processes (N) in which phonon momentum is not changed by scattering and Umklapp processes (U) that change phonon momentum. Normal processes dominate in the low-temperature regime. In contrast, U processes, such as anharmonic phonon-phonon and phonon-electron interactions, typically dominate in the high-temperature regime. Built on the Klemens model, Callaway argued that the total crystal momentum was conserved in N processes, which led to the conclusion that N processes do not contribute to thermal conduction. Callaway modified the initial model to capture the linear relationship between group velocity and the frequency distribution of acoustic phonons [36]. This enabled prediction of thermal conductivity in temperature regimes in which the Debye model accurately captured the phonon frequency distribution (i.e., the low-temperature regime). However, the Debye-Callaway model is not accurate at intermediate temperatures because of inaccuracies in the predictions of the underlying Debye model in this temperature regime.

First-principles calculations can be used to improve the accuracy of the Debye-Callaway model in the intermediate temperature regime by directly determining phonon group velocities and frequency distributions. Using this methodology, intrinsic thermal conductivities have been predicted for γ-Si_3N_4, γ-Ge_3N_4 [37], ZrB_2 [38], copper antimony selenium, and tin-selenium compounds [39]. For example, this methodology predicted a lattice thermal conductivity of about 300 $W\ m^{-1}\ K^{-1}$ for γ-Si_3N_4 at room temperature, which is only ~50 % higher than the highest experimentally measured value [40,41]. In contrast, the Slack model predicted a lattice thermal conductivity of 80 $W\ m^{-1}\ K^{-1}$ [42] for the same material, which is less than half of the highest experimental value. Hence, utilizing first-principles calculations to determine phonon vibration frequency distributions improves the accuracy of the Debye-Callaway model in the intermediate temperature regime.

Up to now, this methodology has not been used to predict the thermal conductivity of ZrC_x ceramics. The purpose of the present study is to use a combination of first-principles calculations and the Debye-Callaway model to predict the lattice thermal conduc-

tivities of ZrC_x with different carbon stoichiometries. The result of this study is not only useful in explaining the origin of discrepancies in experimentally measured thermal conductivities but also can be used as a guideline for tuning the thermal properties of ZrC_x ceramics.

2. Calculation methods

2.1. Lattice thermal conductivity

The total thermal conductivity (κ_{total}) of ZrC_x arises from both electron (κ_e) and lattice (κ_L) contributions, $\kappa_{total} = \kappa_e + \kappa_L$. The magnitude of the electron contribution can be estimated using the Wiedemann-Franz law [43], $\kappa_e = \frac{L_0 T}{\rho}$, where $L_0 = 2.45 \times 10^{-8}$ W Ω^{-1} K^{-2} is the theoretical Lorenz number. Previous studies suggested that κ_L was the dominant contribution to κ_{total} of ZrC_x at lower temperatures [44]. In addition, the calculation of the electron contribution using the Wiedemann-Franz law is straight-forward. As a result, κ_L will be the focus of the present study.

A combination of the Debye-Callaway model [45] and first-principles simulations was employed for calculating κ_L of ZrC_x with different carbon stoichiometries (ZrC, $ZrC_{0.75}$, and $ZrC_{0.5}$ which is also called Zr_2C in some studies) at different temperatures. In the Debye-Callaway model, heat is assumed to be transported by acoustic phonon modes because the group velocities of the optical phonons are significantly lower, which means their contribution to total thermal conductivity is small [46,35,47]. Two transverse (TA1 and TA2) and one longitudinal (LA) acoustic phonon branches contribute to κ_L, which can be expressed by Eq. (1):

$$\kappa_L = \kappa_{TA1} + \kappa_{TA2} + \kappa_{LA} \tag{1}$$

The acoustic phonon branches (κ_i, with i represents TA1, TA2 and LA) are the usual Debye-Callaway terms and are expressed by Eqs. (2) and (3):

$$\kappa_{i1} = \frac{1}{3}\frac{k_B^4 T^3}{2\pi^2 \hbar^3 v_i}\int_0^{\frac{\theta_i}{T}} \frac{\tau_C^i(x) x^4 e^x}{(e^x-1)^2}\mathrm{d}x \tag{2}$$

$$\kappa_{i2} = \frac{1}{3}\frac{k_B^4 T^3}{2\pi^2 \hbar^3 v_i}\frac{\left[\int_0^{\frac{\theta_i}{T}} \frac{\tau_C^i(x) x^4 e^x}{(e^x-1)^2}\mathrm{d}x\right]^2}{\int_0^{\frac{\theta_i}{T}} \frac{\tau_C^i(x) x^4 e^x}{\tau_N^i(x)\tau_R^i(x)(e^x-1)^2}\mathrm{d}x} \tag{3}$$

In Eq. (3), k_B is the Boltzmann constant, $\hbar$ is the reduced Planck constant, v_i is the group velocity of the phonons, θ_i is the Debye temperature of the transverse and longitudinal acoustic phonons, respectively, which is determined by $\theta_i = \hbar\omega_{max}/k_B$, where ω_{max} is the maximum frequency of the acoustic phonon branches at the Brillouin zone boundary [48]. The factor x is expressed by $x = \hbar\omega/k_B T$, τ_C is the total relaxation time of the active phonon scattering processes. In Eq. (3), τ_N is the scattering rate for normal phonon processes, while τ_R is the sum of all of the resistive scattering processes. The relationship between the last three factors is $\tau_C^{-1} = \tau_N^{-1} + \tau_R^{-1}$. The total resistive phonon scattering rate (τ_R^{-1}) is the sum of the phonon-phonon Umklapp scattering (τ_U^{-1}), isotope scattering (τ_I^{-1}), grain boundary scattering (τ_B^{-1}), and phonon-vacancy scattering (τ_V^{-1}) rates. The latter was considered only for $ZrC_{0.75}$ since ZrC has no vacancies and the space group for $ZrC_{0.5}$ accounts for carbon vacancies in that structure. The relaxation time of the Umklapp scattering process can be expressed as Eq. (4) [49]:

$$\left[\tau_U^i\right]^{-1} = \frac{\hbar\gamma_i^2}{M v_i^2 \theta_i}\left(\frac{k_B}{\hbar}\right)^2 x^2 T^3 \exp\left(\frac{-\theta_i}{3T}\right) \tag{4}$$

where M is the average mass of atoms in the crystal, γ_i is the Grüneisen parameter of the acoustic phonon branch which is estimated by Eq. (5) [50]:

$$\gamma_i = \frac{\sum \gamma_{i,q} C_i(q)}{\sum C_i(q)} \tag{5}$$

where $\gamma_{i,q}$ is the mode Grüneisen parameter for mode i at wave vector q which is determined by Eq. (6):

$$\gamma_{i,q} = -\frac{\partial \ln\omega_{i,q}}{\partial \ln V} \tag{6}$$

where V is the volume of the unit cell. In Eq. (5), $C_i(q)$ is defined by Eq. (7):

$$C_i(q) = k_B\left(\frac{\hbar\omega_{i,q}}{k_B T}\right)^2 \frac{\exp\left(\frac{\hbar\omega_{i,q}}{k_B T}\right)}{\left[\exp\left(\frac{\hbar\omega_{i,q}}{k_B T}\right)-1\right]^2} \tag{7}$$

Isotope scattering was assumed to be scattering from static imperfections with masses that are different from the host in a perfect crystal structure and is expressed as Eq. (8) [51]:

$$\left[\tau_I^i\right]^{-1} = \frac{V k_B^4 \Gamma}{4\pi\hbar^4 v_L^3} x^4 T^4 \tag{8}$$

where Γ is the phonon-scattering parameter of the mass-fluctuation which can be calculated by Eqs. (9) and (10):

$$\Gamma = \sum_j c_j\left[\frac{m_j - \overline{m}}{\overline{m}}\right]^2 \tag{9}$$

$$\overline{m} = \sum_j c_j m_j \tag{10}$$

where c_j is the fractional atomic natural abundance of the isotope with atomic mass, m_j. Scattering from Zr isotopes is also considered in the present work using analysis similar to Eqs. (8) and (9). The abundance of the isotopes is assumed to be 51.45 wt.% ^{90}Zr, 11.22 wt.% ^{91}Zr, 17.15 wt.% ^{92}Zr, 17.38 wt.% ^{94}Zr, and 2.80 wt.% ^{96}Zr.

Grain boundary scattering was assumed to be independent of temperature and phonon frequency and only dependent on group velocity and grain diameter [40] as shown by Eq. (11):

$$\left[\tau_B^i\right]^{-1} = \frac{v_i}{d} \tag{11}$$

where d is the effective diameter of the ZrC_x grains.

Phonon-vacancy scattering was assumed to occur due to the atomic mass and radius differences when vacancies form in a crystal structure [52] as described by Eq. (12):

$$[\tau_V]^{-1} = \sum_i f_i\left(1 - \frac{m_i}{\overline{m}}\right)^2 + \sum_i f_i\left(1 - \frac{r_i}{\overline{r}}\right)^2 \tag{12}$$

where f_i is the ratio of vacancy, $\overline{m}$ and m_i are the average mass before and after the vacancy formed, $\overline{r}$ and r_i are the average atomic radius before and after the vacancy formed. As noted previously, phonon-phonon scattering was considered to be a U process and its effect on lattice thermal conductivity is determined using the Callaway model as shown in Eq. (13) [33]:

$$\left[\tau_N^L\right]^{-1} = \frac{V k_B^5 \gamma_L^2}{M\hbar^4 v_T^5} x^2 T^5 \tag{13}$$

The phonon group velocity is defined by Eq. (14):

$$v_g(i, q) = \frac{\partial\omega(i, q)}{\partial q} \tag{14}$$

where the gradient of the dispersion curve at Γ is the group velocity.

2.2. First-principles calculations

ZrC crystallizes in rock salt structure with a space group of $Fm\bar{3}m$ (No. 225) (Fig. 2(a)). The lattice parameter is a =4.699 Å [22]. Zr and C atoms are located at (0, 0, 0) and (0.5, 0.5, 0.5), respectively. The crystal structure of $ZrC_{0.75}$ was built by removing one C atom from the $1\times1\times1$ unit cell of ZrC, as shown in Fig. 2(b), which results in ordered vacancies for the $ZrC_{0.75}$ structure at the scale of the unit cell. The carbon vacancy ordered crystal structure Zr_2C was used for $ZrC_{0.5}$, which was built according to a Rietveld refined structure from the X-ray diffraction pattern [53]. The space group is $Fd\bar{3}m$ (No. 227) and the lattice parameter is a =9.399 Å. The Zr and C atoms are located at (0.3702, 0.3702, 0.3702) and (0.1250, 0.1250, 0.1250) positions, respectively, as shown in Fig. 2(c). This structure is essentially a $2\times2\times2$ super cell of the ZrC unit cell, but with an ordered array of carbon vacancies that requires the larger super cell to fully describe the ordering.

Quantum espresso (QE) [54] was employed to perform the density functional theory (DFT) calculations. Crystal structures were optimized using the Broyden-Fletcher-Goldfarb-Shanno (BFGS) scheme to minimize the total energy and interatomic force [55]. The criteria for convergence in optimizing lattice parameters and internal atom positions were total energy differences within 0.1 mRy atom^{-1}. Vanderbilt-type ultrasoft pseudopotentials [56] were employed to represent the interactions between atom cores and valence electrons. The exchange-correlation energy was treated under the generalized-gradient approximation (GGA) [57] based on the Perdew-Burke-Ernzerhof (PBE) scheme. The cutoff ; of kinetic energy for wavefunctions were fixed at 70 Ry in structure relaxation and self-consistent calculations after convergence tests for all structures. Brillouin zone sampling integration was conducted by the Monkhorst-Pack method [58] with a k-points mesh separation of 0.04 Å^{-1}. Elastic constants were calculated for all three compositions (ZrC, $ZrC_{0.75}$ and $ZrC_{0.5}$). A finite value of homogeneous deformation was generated for calculating the required stress. The three independent symmetry elements, c_{11}, c_{12} and c_{44} of the cubic structure were generated for estimating the polycrystalline shear modulus G and bulk modulus B according to the Voigt-Reuss-Hill approximation [59]. The Young's modulus E, Poisson's ratio ν and microhardness H_V were calculated based on shear modulus G and bulk modulus B according to the following relationships for isotropic materials [60]:

$$E = \frac{9BG}{3B+G} \tag{16}$$

$$\nu = \frac{3B-2G}{2\times(3B+G)} \tag{17}$$

$$H_V = 2\times\left(\frac{G^3}{B^2}\right)^{0.585} - 3 \tag{18}$$

In Eq. (18), microhardness has a unit of GPa, which must also be used for G and B in this calculation. Phonon frequencies as functions of Brillouin zone directions were conducted using density functional perturbation theory (DFPT) [61] with a $9\times9\times9$, $6\times6\times6$, and $5\times5\times5$ k-points mesh for ZrC, $ZrC_{0.75}$, and $ZrC_{0.5}$, respectively. In the phonon calculations within the quasi harmonic approximation (QHA), the cell volume was varied by less than ±1% with respect to the equilibrium cell volume of ZrC, $ZrC_{0.75}$ and $ZrC_{0.5}$.

3. Results and discussion

3.1. Lattice parameters, elastic constants, and mechanical properties

Lattice parameters of ZrC, $ZrC_{0.75}$ and $ZrC_{0.5}$ were calculated in the present study and are compared in Table 2. The lattice parameter of $ZrC_{0.75}$ was 4.692 Å, which was smaller than the lattice parameter of 4.706 Å for ZrC due to the presence of the carbon vacancies. The lattice parameter of $ZrC_{0.5}$ was larger than those for ZrC and $ZrC_{0.75}$ since the crystal structure contains 48 atoms compared to 8 atoms for ZrC and 7 atoms for $ZrC_{0.75}$. However, the average distance between two neighboring Zr atoms along the crystallographic axes was 4.717 Å, which is analogous to the lattice parameter for the other two structures. The lattice expanded for $ZrC_{0.5}$ in contrast to the trend from ZrC to $ZrC_{0.75}$. The lattice parameter decreased as carbon vacancy content increased initially due to the loss of carbon atoms that resulted in shrinkage of the structure. However, when the carbon vacancy content reaches about 20 % (i.e., $ZrC_{0.8}$), the average distance between Zr atoms begins to increase due to the decrease in bond strength that results from the increasing metallic bond character with increasing carbon vacancy content [62].

Elastic properties are direct reflection of chemical bonding. Table 2 tabulates the elastic constants and microhardness of ZrC, $ZrC_{0.75}$ and $ZrC_{0.5}$. Data from previous publications are also included for comparison. The calculated mechanical properties of ZrC and $ZrC_{0.5}$ are consistent with the values from previous studies. For example, the second-order elastic constants c_{11}, c_{44} and c_{12} of ZrC are 451.6 GPa, 155.4 GPa and 106.9 GPa, respectively, which are very close to corresponding values of 451.6 GPa, 155.3 GPa and 106.9 GPa calculated in a previous report [63], demonstrating the reliability of present calculations. The bulk modulus B, shear modulus G and elastic modulus E of polycrystalline ZrC_x all decrease with increasing carbon vacancy content. For example, G decreases from 162.2 GPa for ZrC to 119.5 GPa $ZrC_{0.75}$, and 82.1 GPa for $ZrC_{0.5}$. Correspondingly, H_V decreases from 24.2 GPa for ZrC to 16.2 GPa for $ZrC_{0.75}$ and 11.7 GPa for $ZrC_{0.5}$. In contrast, Poisson's ratio increases with increasing carbon vacancy content from 0.21 for ZrC to 0.25 for $ZrC_{0.5}$, indicating a decrease in average bond strength as carbon atoms are removed from the structure.

3.2. Phonon dispersions and vibration properties

Phonon dispersion curves for ZrC are shown in Fig. 3(a). The primitive ZrC cell contains one Zr atom and one C atom, which result in six phonon branches, i.e., three acoustic (colored lines) and three optical (black lines). No imaginary frequencies were predicted in any of the high-symmetry directions in the Brillouin zone, indicating the dynamic stability of ZrC under perturbation. The apparent gap between the acoustic phonon branches and optical phonon branches (>5 THz at the L point) is due to anisotropic bonding and mass differences between Zr and C in ZrC. These results also suggest that the contribution of the optical modes to the thermal conductivity of ZrC is negligible due to the significantly higher frequencies, as has been demonstrated in ZrB_2 by Xiang et al. [42].

The phonon group velocities for TA1, TA2, and LA of ZrC are 4.2 km s^{-1}, 4.2 km s^{-1} and 8.0 km s^{-1}, respectively, in the Γ-X direction (Table 3). Since spectral thermal conductivity is proportional to the square of the phonon group velocity, $\kappa_s(\omega) = C_s(\omega)V_g(\omega)^2\tau(\omega)$ [38], the higher group velocities are an indication of higher thermal conductivity for ZrC. Thermal conductivity is also proportional to the phonon relaxation time [39], which is the mean time between scattering events attributed to the various resistive processes. The phonon relaxation time can be determined from the mode

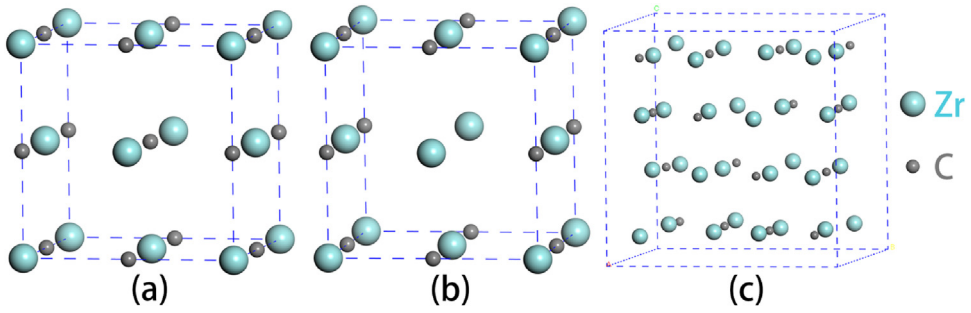

Fig. 2. Crystal structures of (a) ZrC, (b) $ZrC_{0.75}$ and (c) Zr_2C ($ZrC_{0.5}$).

Table 2
Calculated lattice parameters (a), elastic constants (c_{11}, c_{44}, c_{12}), shear modulus (G), bulk modulus (B), elastic modulus (E), Poisson's ratio (ν), and microhardness (H_V) of ZrC, $ZrC_{0.75}$ and Zr_2C ($ZrC_{0.5}$) in the present and (previously reported) calculations.

Composition	Lattice constant a (Å)	c_{11} (Gpa)	c_{44} (GPa)	c_{12} (GPa)	G (GPa)	B (GPa)	E (GPa)	ν	H_V (GPa)
ZrC	4.706, (4.705) [63]	451.6, (451.6) [63]	155.4, (155.3) [63]	106.9, (106.9) [63]	162.2, (162.1) [63]	221.8, (221.8) [63]	391.2, (390.7) [63]	0.21, (0.206) [61]	24.2, (23.4) [22], (24.3) [22]
$ZrC_{0.75}$	4.692	369.2	108.9	98.4	119.5	188.6	295.9	0.24	16.2
Zr_2C ($ZrC_{0.5}$)	9.369 [22]	205.3	101.6	100.0	82.1, (71) [22]	135.1, (137) [22]	204.7	0.25	11.7, (8.4) [22], (10.8) [23]

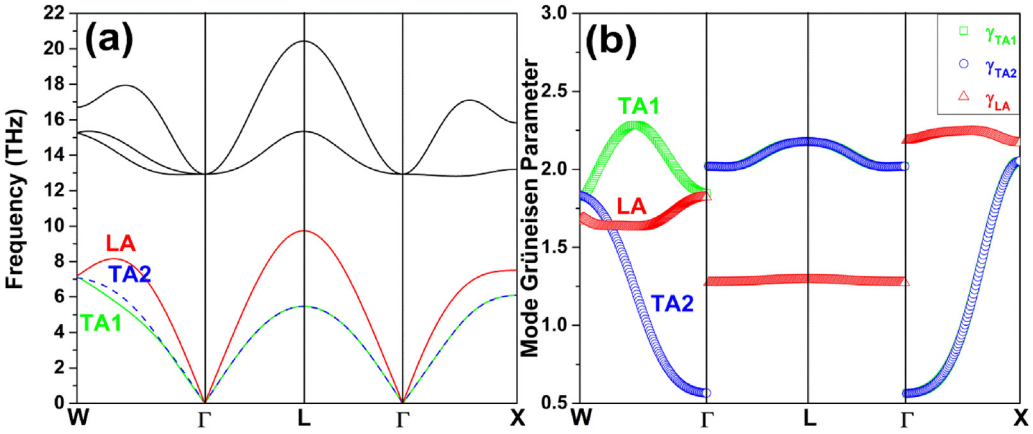

Fig. 3. Phonon dispersion (a) and mode Grüneisen parameters (b) of ZrC.

Table 3
Grüneisen parameters, Debye temperatures, and group velocities of ZrC, $ZrC_{0.75}$ and Zr_2C ($ZrC_{0.5}$) compared with a highly thermal conductive (ZrB_2) [37] and thermal insulating rare-earth pyrochlores [64].

Composition	γ_{TA1} N/A	γ_{TA2}	γ_{LA}	θ_{TA1} (K)	θ_{TA2}	θ_{LA}	v_{TA1} (km s^{-1})	v_{TA2}	v_{LA}
ZrC	1.79	1.51	1.65	340	340	467	4.2	4.2	8.0
$ZrC_{0.75}$	0.92	1.28	1.52	242	242	242	2.4	2.4	3.2
Zr_2C	10.05	9.12	4.32	167	172	220	4.0	4.8	7.1
ZrB_2	1.50	1.22	1.43	380	355	422	6.5	6.5	9.2
$Nd_2Zr_2O_7$	6.23	10.10	2.75	138	138	260	3.13	3.13	5.91
$Sm_2Zr_2O_7$	7.40	11.98	2.81	137	137	256	3.09	3.09	5.78
$Gd_2Zr_2O_7$	7.19	11.57	2.75	137	137	252	3.06	3.06	5.63

Grüneisen parameters, γ_i, which is related to the anharmonicity of the phonon vibrations and plays an important role in thermal conductivity. The mode Grüneisen parameters are calculated using harmonic lattice dynamic calculations over a range of volumes around the equilibrium state using Eq. (6). As shown in Fig. 3(b), the mode Grüneisen parameters of ZrC are positive across the Brillouin zone, which implies that ZrC is stable in the rock salt structure at elevated pressures.

Fig. 4(a) shows the phonon dispersion curves for $ZrC_{0.75}$. Compared to ZrC, the phonon dispersion curves for $ZrC_{0.75}$ contain additional optical phonon modes at frequencies between ~6 THz and ~8 THz, which are due to the presence of carbon vacancy. These moderate frequency optical phonons scatter acoustic phonons (i.e., phonon-phonon scattering), especially the longitudinal acoustic phonon branch. The scattering of acoustic phonons results in reduced group velocities as can be seen from the gradient of the dispersion curve at the Γ points in Fig. 4(a) and the data in Table 3.

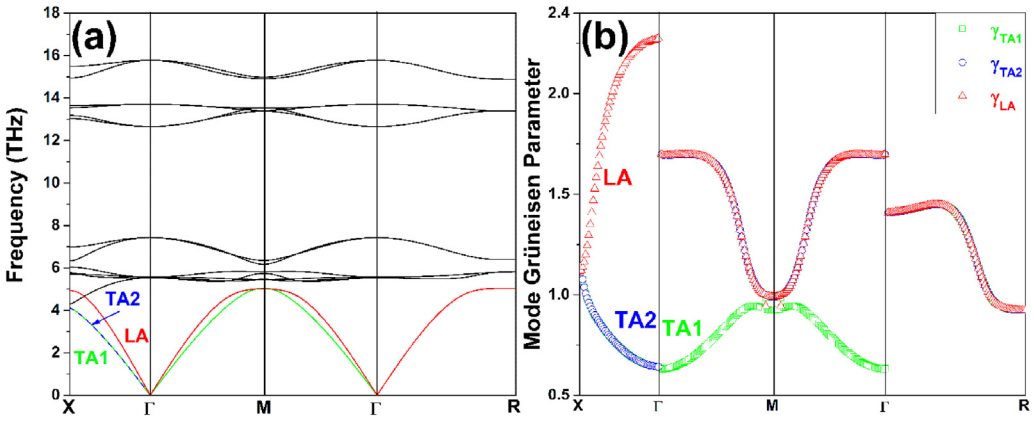

Fig. 4. Phonon dispersion (a) and mode Grüneisen parameters (b) of $ZrC_{0.75}$.

In addition, the scattering of acoustic phonons by the moderate frequency optical phonons also decreases the Debye temperature and increases the longitudinal acoustic mode Grüneisen parameter compared to ZrC (Fig. 4(b)). Since the Debye temperature is determined by the maximum frequency of the acoustic branches at the Brillouin zone boundary, a decrease in the Debye temperature is reasonable (Table 3) based on Figs. 3 and 4. For example, θ_{TA1} and θ_{TA2} decrease from 340 K for ZrC to 242 K for $ZrC_{0.75}$, while θ_{LA} decreases from 467 K for ZrC to 242 K for $ZrC_{0.75}$. As a consequence, scattering of acoustic phonons by the moderate frequency optical phonons is active in $ZrC_{0.75}$, but not in ZrC, which should decrease the lattice thermal conductivity of $ZrC_{0.75}$.

When more carbon atoms were removed from the structure and $ZrC_{0.5}$ formed, more optical phonon modes were active at frequencies between ~4 THz and ~8 THz, as can be seen from the phonon dispersion curves shown in Fig. 5(a). The number of these moderate frequency optical modes increased from 0 for ZrC to 9 for $ZrC_{0.75}$, and 21 for $ZrC_{0.5}$. Scattering of acoustic phonons by these low-lying optical phonons resulted in lower group velocities, which were v_{TA1} = 4.0 km s^{-1}, v_{TA2} = 4.8 km s^{-1} and v_{LA} = 7.1 km s^{-1} (as can be seen from the reduced gradient of the dispersion curve at the Γ points in Fig. 5(a) and Table 3). In addition, the mode Grüneisen parameters of the acoustic branches were very large with TA1 and TA2 values of more than 22 and LA of more than 5 (Fig. 5(b)). Since the mode Grüneisen parameter is a measure of lattice vibration anharmonicity, the large values indicate that the phonon thermal conductivity of $ZrC_{0.5}$ will be much lower than ZrC or $ZrC_{0.75}$ due to the increased anharmonicity. The longitudinal acoustic phonon branches and the moderate frequencies optical phonon branches overlapped due to scattering of optical phonons by carbon vacancies. The frequencies of the acoustic phonon branches for $ZrC_{0.5}$ were lower than those for $ZrC_{0.75}$, so the Debye temperatures decreased as well (Table 3). For example, θ_{TA1} and θ_{TA2} decreased from 242 K for $ZrC_{0.75}$ to 167 K and 172 K for $ZrC_{0.5}$, respectively while θ_{LA} decreased from 242 K for $ZrC_{0.75}$ to 220 K for $ZrC_{0.5}$. The reduction in the Debye temperature for ZrC_x with increasing carbon vacancy content is consistent with previous studies [22].

3.3. Grüneisen parameters

The Grüneisen parameters (γ_i), Debye temperatures (θ_i) and group velocities (v_i) of the acoustic phonon branches (Table 3) are the determinant parameters for calculating the phonon thermal conductivity. The changes in the thermal properties of ZrC_x can be summarized by comparing the Grüneisen parameters and Debye temperatures with materials that have high lattice thermal conductivities, such as ZrB_2 [35], and low lattice thermal conductivities, such as rare-earth pyrochlore materials [50]. Grüneisen parameters and Debye temperatures of ZrC are close to ZrB_2 (for example, γ_{TA1} values are 1.79 and 1.50, θ_{TA1} values are 340 K and 380 K for ZrC and ZrB_2 [35], respectively) as presented in Table 3. As the carbon vacancy content increases, the values of the Grüneisen parameters and Debye temperatures tend to change toward representative low lattice thermal conductivity materials such as $Gd_2Zr_2O_7$ [64]. Hence, the lattice thermal conductivity of ZrC_x should decrease to values similar to thermal insulators as the carbon vacancy content increases. This result is intriguing since it implies that the thermal conductivity of ZrC_x can be tuned from a high thermal conductivity/thermal dissipating material to a low thermal conductivity/thermal insulating material through controlling the composition and carbon vacancy content. From this angle, the lattice thermal conductivity can be increased with high x such as ZrC and decreased with low x such as $ZrC_{0.5}$.

3.4. Thermal conductivity

The temperature-dependent lattice thermal conductivities of ZrC, $ZrC_{0.75}$ and $ZrC_{0.5}$ predicted using the Debye-Callaway model are shown in Fig. 6. The initial simulations predicted lattice thermal conductivities, labeled κ_{UI} in Fig. 6, of 122 W m^{-1} K^{-1} for ZrC, 33 W m^{-1} K^{-1} for $ZrC_{0.75}$, and 3 W m^{-1} K^{-1} for $ZrC_{0.5}$, considering the natural abundance of Zr isotopes. From these simulations, the lattice thermal conductivity of ZrC_x decreases with the increasing carbon vacancy content. This decreasing trend is consistent with expectations based on trends in the Grüneisen parameters and Debye temperatures discussed above. The significant change of lattice thermal conductivity opens a new window to tailor the thermal conductivity of ZrC_x through composition and carbon vacancy control. However, the predicted values of ZrC and $ZrC_{0.75}$ are higher than the experimental values for total thermal conductivity at room temperature, which are less than 30 W m^{-1} K^{-1} for ZrC_x with low (but not well-characterized) carbon vacancy contents. One reason that the predicted lattice thermal conductivity values are higher than measured values for ZrC_x ceramics is that the simulations assumed perfect crystal structure without any impurities or defects. In addition, other possible scattering mechanisms may also need to be considered to decrease the predicted values and make them more realistic compared to experimental values. For ZrC, the room temperature lattice thermal conductivity decreased from 122 W m^{-1} K^{-1} when only considering isotope effects (κ_{UI}) to 100 W m^{-1} K^{-1} when considering isotope and grain boundary effects (κ_{UA}), and 68 W m^{-1} K^{-1} when considering isotope and grain boundary effects along with N and U scattering processes (κ_N). Even with these effects, the room temperature thermal conductivity of ZrC is still about twice of the experimental value, so other scattering mechanisms may have a significant impact on the lattice thermal

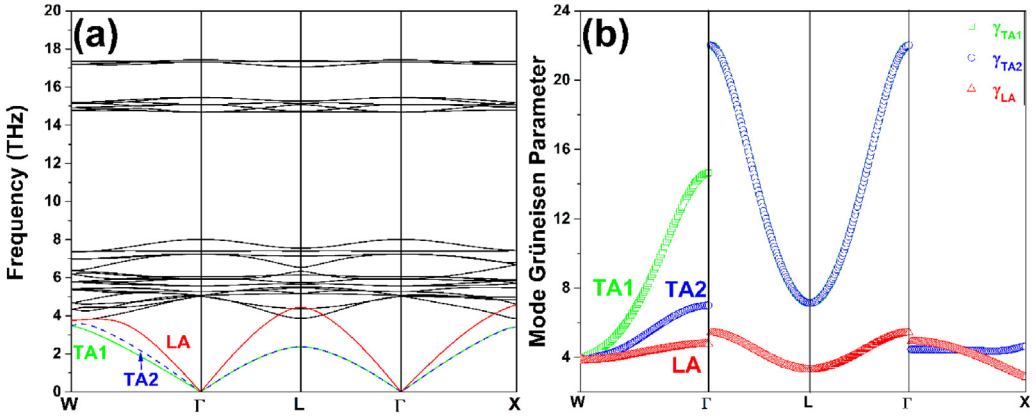

Fig. 5. Phonon dispersion (a) and mode Grüneisen parameters (b) of Zr_2C ($ZrC_{0.5}$).

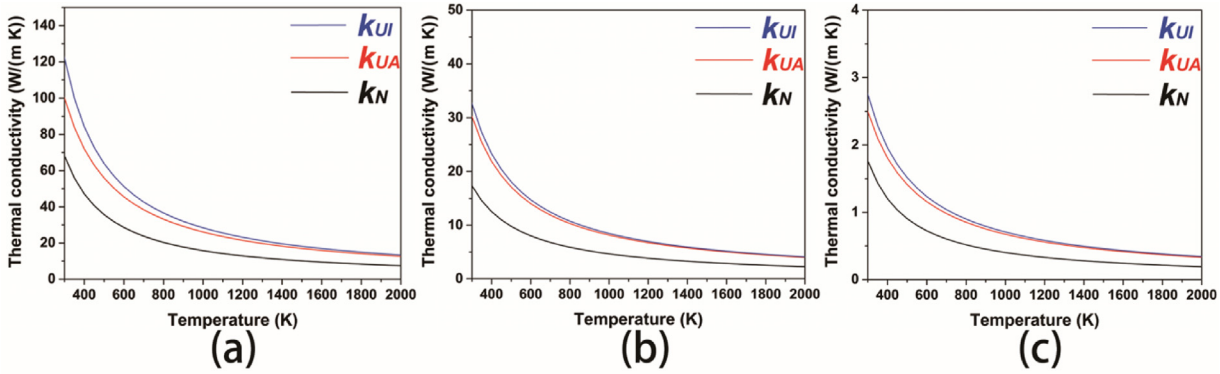

Fig. 6. Lattice thermal conductivities of (a) ZrC, (b) $ZrC_{0.75}$ and (c) Zr_2C ($ZrC_{0.5}$) based on theoretical prediction. (κ_{UI}: isotope effect; κ_{UA}: isotope and grain boundary effects; κ_N: isotope, grain boundary, U, and N effects.).

conductivity of ZrC_x ceramics. The simulations may also predict values that are too high since the sizes of the cells in the simulations were not large enough to capture the effects of random carbon vacancies (i.e., the simulations include the implicit assumption that the carbon vacancies are ordered). Hence, simulations provide an upper bound for possible thermal conductivity values.

The lattice thermal conductivities decreased as temperature increased due to the increased phonon-phonon scattering [4]. When temperature is much higher than the Debye temperature, the number of phonons becomes proportional to temperature, and phonon-phonon interreactions increase significantly. For ZrC, the lattice thermal conductivity (κ_N) was 68 W m^{-1} K^{-1} at room temperature, and decreased to 7 W m^{-1} K^{-1} when temperature increased to 2000 K. The trend in the present study consists with a previous experimental result wherein the phonon contribution to thermal conductivity was obtained by taking the experimentally measured total thermal conductivity for ZrC_x with x values approaching 1 and subtracting the electron contribution to thermal conductivity that was calculated using the Wiedemann-Franz law [40]. The total thermal conductivity of ZrC_x increases with increasing temperature, as shown in Fig. 1, and the high-temperature thermal conductivity is dominated by electron conductivity. In contrast to simulations, experimental measurements should be considered a lower bound for thermal conductivity because of the presence of grain boundaries, dissolved impurities, second phases, and other features that decrease the measured value compared to the inherent thermal conductivity of the material.

Lattice thermal conductivity can either be limited by extrinsic effects (e.g., isotopes, impurities, point defects, or grain boundary scattering) [65] or intrinsic effects (e.g., phonon-phonon scattering) [66]. Grain size is an extrinsic effect that decreases thermal conductivity because phonons are scattered by grain boundaries [29,67,68], thus lattice thermal conductivity decreases as the number of grain boundaries increases with decreasing grain size [69,70]. To quantify this effect, lattice thermal conductivities with grain sizes of 1 μm, 5 μm and 20 μm were calculated for all compositions as shown in Fig. 7. For example, lattice thermal conductivity was 78 W m^{-1} K^{-1} for ZrC with a grain size of 1 μm, 100 W m^{-1} K^{-1} for a grain size of 5 μm, and 110 W m^{-1} K^{-1} for a grain size of 20 μm. Similar trends were also predicted for $ZrC_{0.75}$ and $ZrC_{0.5}$. The calculations correctly predicted that lattice thermal conductivity decreased with decreasing grain size due to increasing phonon scattering at grain boundaries. However, the magnitude of this effect is not sufficient to explain the lattice thermal conductivity values typically measured experimentally for ZrC_x ceramics.

The presence of mixed isotopes also affects lattice thermal conductivity, resulting in a decrease in thermal conductivity when the natural abundance of isotopes was considered [71–76]. For example, the thermal conductivity of $^{11}B_4{}^{12}C$ was about 15 % lower than $^{10}B_4{}^{12}C$ at room temperature [57] and is further lowered when mixtures of isotopes were considered. The heavier isotopes play a critical role in scattering. For some materials that have large mass differences between isotopes, phonon-isotope scattering can dominate the overall thermal conductivity (i.e., overwhelm phonon-phonon scattering) at room or elevated temperatures. For example, the thermal conductivity of GaN with a natural abundance of isotopes is about 33 % lower than the isotopically pure GaN at room temperature due to weak anharmonic phonon-phonon scattering [60]. Strong isotope-phonon scattering and weak anharmonic phonon-phonon scattering result in a large isotope effect

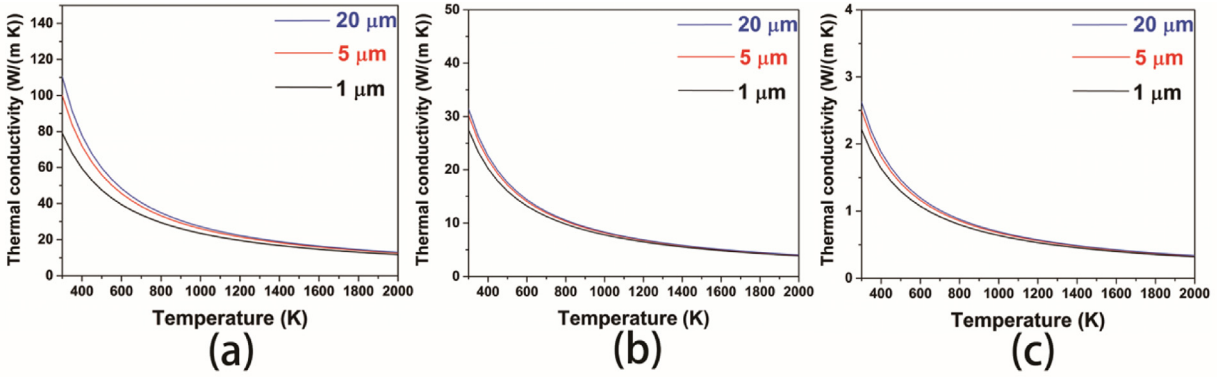

Fig. 7. Lattice thermal conductivities of (a) ZrC, (b) $ZrC_{0.75}$ and (c) Zr_2C ($ZrC_{0.5}$) with different grain sizes.

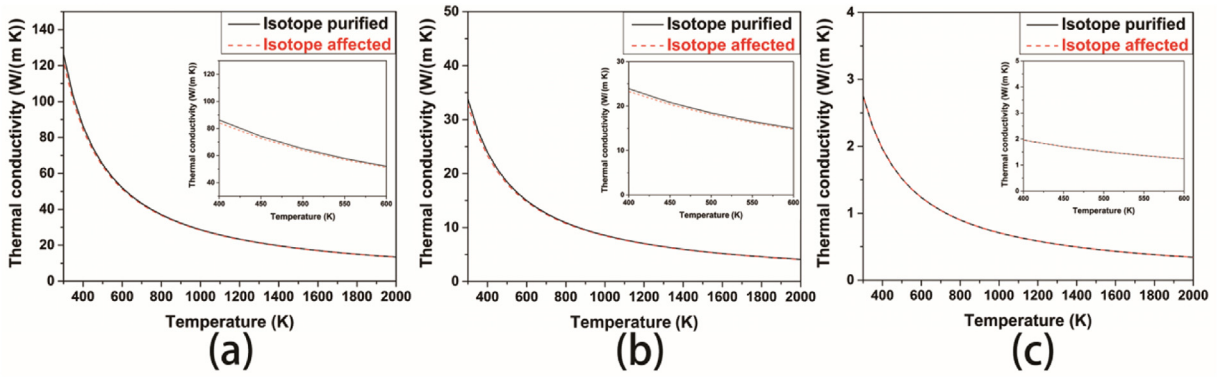

Fig. 8. Isotopopically pure and natural abundance isotope lattice thermal conductivities of (a) ZrC, (b) $ZrC_{0.75}$ and (c) Zr_2C ($ZrC_{0.5}$).

on the vibrational properties. The isotope effect on lattice thermal conductivity of ZrC was calculated previously [29], which showed that isotope scattering can be the predominant effect in determining lattice thermal conductivity. However, the isotope effect is temperature-dependent and its effectiveness decreases as temperature increases. In the present work, the effect of isotopes on the lattice thermal conductivities of ZrC_x ceramics was minimal as shown in Fig. 8. For example, accounting for the natural abundance of Zr isotopes only reduced room temperature lattice thermal conductivity from 126 W m^{-1} K^{-1} when the effect was not considered to 122 W m^{-1} K^{-1} when isotope effect was considered. Based on these analyses, isotope scattering is also not sufficient to account for the lower experimental values of thermal conductivity.

3.5. Mechanism of low lattice thermal conductivity

The combination of the Debye-Calloway model and first principles computations correctly predicted trends for the lattice thermal conductivity of ZrC_x with temperature and carbon vacancy content. However, the predicted lattice thermal conductivity values for ZrC and $ZrC_{0.75}$ are higher than measured total thermal conductivity values, so additional research will examine other possible mechanisms to explain the differences. As discussed above, part of the difference is due to the effects of defects such as impurities or pores in real materials that reduce the measured thermal conductivity of real materials compared to the inherent value. All of these defects scatter the phonons or otherwise impede thermal transport. Common impurities in zirconium carbide include Hf, O, and N. All Zr-based materials made from commercial Zr sources contain Hf due to its presence in naturally-occurring Zr minerals and the difficulty associated with separating Zr and Hf. The presence of Hf impurities could decrease the thermal conductivity of ZrC significantly. Zirconium carbide also typically contains dissolved O and N that substitute onto carbon vacancy sites. These factors could lower experimental values of thermal conductivity compared to the present results, which do not take those factors into account. Similarly, pores could also reduce the thermal conductivities significantly. ZrC_x samples with lower relative densities have relatively lower thermal conductivities as listed in Table 1 and shown in Fig. 1. In addition, the high x value in the bulk ZrC_x sample is 0.98 instead of 1. Thus the measured values are lower than the inherent thermal conductivity, and simulations likely overestimate thermal conductivity since not all scattering mechanisms are considered. Future simulations could consider additional factors such as grain boundary resistance or phonon-electron scattering, which may be active in real materials and could reduce the predicted values. Once lattice thermal conductivity values are within the range expected based on experimental studies, then the effects of electron thermal conductivity can be combined with lattice thermal conductivity predictions to more fully analyze total thermal conductivity of zirconium carbide ceramics.

4. Conclusion

The lattice thermal conductivities have been predicted for ZrC_x with different carbon vacancy contents (ZrC, $ZrC_{0.75}$ and $ZrC_{0.5}$). Phonon frequencies were calculated as a function of Brillouin zone direction using the finite displacement method. In addition, the Grüneisen parameters, Debye temperatures, and group velocities were determined. The properties calculated from first principles predictions are consistent with other studies and were subsequently used as inputs to the Debye-Callaway model to determine lattice thermal conductivity. The lattice thermal conductivities of ZrC_x with different carbon vacancy contents all decrease

as temperature increases due to the effect of phonon-phonon scattering. Lattice thermal conductivities of ZrC_x also decreased with increasing carbon vacancy content because increasing carbon vacancy content decreases the vibration frequencies, which causes a decreased ability to transport heat. Thus, ZrC_x can be tailored from a thermal dissipating material with $x \approx 1$ to a thermal insulating material when $x = 0.5$, which opens a new window to tune the thermal conductivity of ZrC_x through carbon vacancy control. The effects of the natural distribution of Zr isotopes, grain boundaries, and phonon-phonon interactions all decrease the lattice thermal conductivities for all of the compositions studied in this work. While these calculations correctly predict the trends in lattice thermal conductivity with temperature, the magnitudes of the values predicted for ZrC are higher than experimentally measured total thermal conductivity values. Hence, future research will focus on incorporating additional mechanisms to account for differences between predicted lattice thermal conductivity values and those typically measured for ZrC_x ceramics.

Declaration of Competing Interest

The authors report no declarations of interest.

Acknowledgements

This work was supported by the Ceramics Program in the U.S. National Science Foundation (DMR 1742086). The computational efforts, for the first principle calculations, were assisted by the National Supercomputing Center in Shenzhen, China.

References

[1] S. Ueta, J. Aihara, A. Yasuda, H. Ishibashi, T. Takayama, K. Sawa, J. Nucl. Mater. 376 (2008) 146–151.
[2] G.D. Del Cul, B.B. Spencer, C.W. Forsbert, E.D. Collings, W.S. Rickman, Trans. Am. Nucl. Soc. 88 (2003) 376.
[3] E. López-Honorato, J. Tan, P.J. Meadows, G. Marsh, P. Xiao, J. Nucl. Mater. 392 (2009) 219–224.
[4] T. Ogawa, K. Ikawa, J. Nucl. Mater. 98 (1981) 18–26.
[5] G. Newsome, L.L. Snead, T. Hinoki, Y. Katoh, D. Peters, J. Nucl. Mater. 371 (2007) 76–89.
[6] L.L. Snead, Y. Katoh, S. Kondo, J. Nucl. Mater. 399 (2010) 200–207.
[7] G.M. Song, Y.J. Wang, Y. Zhou, J. Mater. Sci. 36 (2001) 4625–4631.
[8] Q. Tong, J. Shi, Y. Song, Q. Guo, L. Liu, Carbon 42 (2004) 2495–2500.
[9] M.B. Dickerson, P.J. Wurm, J.R. Schorr, W.P. Hoffman, P.G. Wapner, K.H. Sandhage, J. Mater. Sci. 39 (2004) 6005–6015.
[10] X.T. Shen, L. Liu, W. Li, K.Z. Li, Ceram. Int. 41 (2015) 11793–11803.
[11] Q. Liu, J. Liu, X. Luan, J. Mater. Sci. Technol. 35 (2019) 2942–2949.
[12] C.C. Sorrell, V.S. Stubican, R.C. Bradt, J. Am. Ceram. Soc. 69 (1986) 317–321.
[13] L. Xu, C. Huang, H. Liu, B. Zou, H. Zhu, G. Zhao, J. Wang, Int. J. Refract. Met. Hard Mater. 37 (2013) 98–105.
[14] Y. Xu, W. Sun, X. Xiong, F. Liu, X. Luan, J. Mater. Sci. Technol. 35 (2019) 2785–2798.
[15] R.E. Taylor, J. Am. Ceram. Soc. 45 (1962) 74–78.
[16] B. Wei, L. Chen, Y. Wang, H. Zhang, S. Peng, J. Ouyang, D. Wang, Y. Zhou, J. Eur. Ceram. Soc. 38 (2018) 411–419.
[17] X. Wei, C. Back, O. Izhvanov, C. Haines, E. Olevsky, Materials 9 (2016) 577.
[18] R.E. Taylor, J. Morreale, J. Am. Ceram. Soc. 47 (1964) 69–73.
[19] L.N. Grossman, J. Am. Ceram. Soc. 48 (1965) 236–242.
[20] R.V. Sara, J. Am. Ceram. Soc. 48 (1965) 243–247.
[21] Y. Katoh, G. Vasudevamurthy, T. Nozawa, L.L. Snead, J. Nucl. Mater. 441 (2013) 718–742.
[22] C.W. Xie, A.R. Oganov, D. Li, T.T. Debela, N. Liu, D. Dong, Q.F. Zeng, Phys. Chem. Chem. Phys. 18 (2016) 12299.
[23] Y.H. Zhang, B. Liu, J.M. Wang, J.Y. Wang, Acta Mater. 111 (2016) 232–241.
[24] J.P. Crocombette,J. Phys. Condens. Matter 25 (2013), 505501.
[25] L.G. Radosevich, W.S. Williams, J. Am. Ceram. Soc. 49 (1966) 156–159.
[26] R.O. Pohl, Phys. Rev. Lett. 8 (1962) 481.
[27] A.I. Gusev, A.A. Rempel, A.J. Magerl, Disorder and Order in Strongly Nonstoichiometric Compounds, Springer, Heidelberg, 2001.
[28] Y. Zhang, B. Liu, J. Wang, Sci. Rep. 5 (2015) 18098.
[29] Y. Zhou, T.W. Heitmann, E. Bohannan, J.C. Schaeperkoetter, W.G. Fahrenholtz, G.E. Hilmas, J. Am. Ceram. Soc. 103 (2020) 2891–2898.
[30] W. Hu, J. Xiang, Y. Zhang, S. Liu, C. Chen, P. Wang, H. Wang, F. Wen, B. Xu, J. He, D. Yu, Y. Tian, Z. Liu, J. Mater. Res. 27 (2012) 1230–1236.
[31] T.A. Mellan, A. Aziz, Y. Xia, R. Grau-Crespo, A.I. Duff,Phys. Rev. B 99 (2019), 094310.
[32] Y. Zhou, T.W. Heitmann, W.G. Fahrenholtz, G.E. Hilmas, J. Eur. Ceram. Soc. 39 (2019) 2594–2600.
[33] E. Padovano, C. Badini, K. Mergia, J. Barcena, Ceram. Int. 44 (2018) 15050–15057.
[34] T.H.K. Barron, G.K. White, Heat Capacity and Thermal Expansion at Low Temperatures, Berlin/Heidelberg, Germany, Springer Science & Business Media, 2012.
[35] P.G. Klemens, Proc. R. Soc. Lond. Ser. A 208 (1951) 108–133.
[36] J. Callaway, Phys. Rev. 113 (1959) 1046–1051.
[37] H. Xiang, Z. Feng, Z. Li, Y. Zhou, Sci. Rep. 8 (2018) 14374.
[38] H. Xiang, J. Wang, Y. Zhou, J. Eur. Ceram. Soc. 39 (2019) 2982–2988.
[39] Y. Zhang, J. Materiomics 2 (2016) 237–247.
[40] K. Hirao, Y. Zhou, H. Hyuga, T. Ohji, D. Kusano, J. Korean Ceram. Soc. 49 (2012) 380–384.
[41] Y. Zhou, H. Hyuga, D. Kusano, Y. Yoshizawa, K. Hirao, Adv. Mater. 23 (2011) 4563–4567.
[42] D. Morelli, J. Heremans, Appl. Phys. Lett. 81 (2013) 8–10.
[43] W. Jones, N.H. March, Theoretical Solid State Physics, John Wiley & Sons, London, Great Britain, 1973.
[44] R.E. Taylor, E.K. Storms, Thermal transport in refractory carbides, in: P.H. Klemens, T.K. Chu (Eds.), Thermal Conductivity 14, Plenum Press, New York, 1975.
[45] D.T. Morelli, J.P. Heremans, G.A. Slack,Phys. Rev. B 66 (2002), 195304.
[46] M. Asen-Palmer, K. Bartkowski, E. Gmelin, M. Cardona, A. Zhernov, A. Inyushkin, A. Taldenkov, V. Ozhogin, K. Itoh, E. Haller, Phys. Rev. B 56 (1997) 9431–9447.
[47] L. Lindsay, D.A. Broido, T.L. Reinecke,Phys. Rev. B 88 (2013), 144306.
[48] H. Xiang, Z. Feng, Z. Li, Y. Zhou, Sci. Rep. 8 (2018) 14374.
[49] D.T. Morelli, J.P. Heremans, G.A. Slack,Phys. Rev. B 66 (2002), 195304.
[50] G. Grimvall, Thermophysical Properties of Materials, Elsevier, Amsterdam, Netherlands, 1999.
[51] P.G. Klemens, Proc. Phys. Soc. Sect. A 68 (1955) 1113–1128.
[52] E.S. Toberer, A. Zevalkink, G.J. Snyder, J. Mater. Chem. 21 (2011) 15843–15852.
[53] W. Hu, J. Xiang, S. Liu, Y. Zhang, C. Chen, P. Wang, H. Wang, Inorg. Chem. 51 (2012) 5164–5172.
[54] P. Giannozzi, S. Baroni, N. Bonini, M. Calandra, R. Car, C. Cavazzoni, D. Ceresoli, G. Chiarotti, M. Cococcioni, I. Dabo,J. Phys. Condens. Matter 21 (2009), 395502.
[55] B.G. Pfrommer, M. Côté, S.G. Louie, M.L. Cohen, J. Comput. Phys. 131 (1997) 233–240.
[56] D. Vanderbilt, Phys. Rev. B 41 (1990), 7892-1895.
[57] J.P. Perdew, K. Burke, M. Ernzerhof, Phys. Rev. Lett. 77 (1996) 3865–3868.
[58] H.J. Monkhorst, J.D. Pack, Phys. Rev. B 13 (1976) 5188–5192.
[59] W. Voigt, Lehrbuch der Kristallohysic, Teubner, Leipzig, Germany, 1928.
[60] X. Chen, H. Niu, D. Li, Y. Li, Intermetallics 19 (2011) 1275–1281.
[61] X. Gonze, Phys. Rev. B 55 (1997) 10337–10354.
[62] H.F. Jackson, W.E. Lee, Properties and characteristic of ZrC, in: R. Konings (Ed.), Stoller Volume 2 in Comprehensive Nuclear Materials, Elsevier, Amsterdam, Netherland, 2012, pp. 339–372.
[63] H. Li, L. Zhang, Q. Zeng, K. Guan, K. Li, H. Ren, S. Liu, L. Cheng, Solid State Commun. 151 (2011) 602–606.
[64] G. Lan, B. Ouyang, J. Song, Acta Mater. 91 (2015) 304–317.
[65] T. Wang, J. Carrete, A. van Roekeghem, N. Mingo, G.K.H. Madsen,Phys. Rev. B 95 (2017), 245304.
[66] J.M. Ziman, Electrons and Phonons: the Theory of Transport Phenomena in Solids, Oxford University Press, Oxford, United Kingdom, 2001.
[67] H.J. Goldsmid, A.W. Penn, Phys. Lett. A 27 (1968) 523–524.
[68] J.E. Parrott, J. Phys. C: Solid State Phys. 2 (1969) 147.
[69] N. Savvides, H.J. Goldsmid, J. Phys. C: Solid State Phys. 13 (1980) 4657–4670.
[70] D.M. Rowe, C.M. Bhandari, Appl. Phys. Lett. 47 (1985) 255–257.
[71] Y. Arita, Y. Nishi, M. Amaya, T. Matsui, Thermochim. Acta 352 (2000) 39–42.
[72] S. Chen, Q. Wu, C. Mishra, J. Kang, H. Zhang, K. Cho, W. Cai, A. Balandin, R. Ruoff, Nat. Mater. 11 (2012) 203–207.
[73] L. Lindsay, D.A. Broido, T.L. Reinecke,Phys. Rev. Lett. 109 (2012), 095901.
[74] L. Lindsay, D.A. Broido, T.L. Reinecke,Phys. Rev. B 87 (2013), 165201.
[75] X. Li, J. Chen, C. Yu, G. Zhang,Appl. Phys. Lett. 103 (2013), 013111.
[76] L. Lindsay, D.A. Broido, T.L. Reinecke,Phys. Rev. B 88 (2013), 144306.